Computation of Backwards-Facing Step-Ramp Induced Shock-Wave Boundary-Layer Interaction

Robert Alviani*, Jonathan Poggie † and Gregory Blaisdell ‡
Purdue University, West Lafayette, IN, 47907

This paper presents a Computational Fluid Dynamic (CFD) investigation of a backwards-facing step-ramp (BFSR) geometry. This geometry is used to represent an idealized wing-elevon cove region for an aircraft. The goal of this project's research is to determine how flow structure and surface variables are affected by adjustments of the characteristic flow parameters. Flow structure consists of shock-wave boundary-layer interaction (SWBLI) and recirculation. Surface variables monitored were the coefficient of skin friction, the Stanton number, and the pressure coefficient. The characteristic flow parameters include boundary-layer thickness, Reynolds number, ramp deflection, Mach number, and altitude. Current computations employ an idealized 2-D geometry, seeking steady-state solutions, utilizing the Reynolds-Averaged Navier-Stokes (RANS) equations and the Spalart-Allmaras (S-A) turbulence model. The overall system produced several trends with variation of flow parameters and geometry of the system. The base case, with no deflection, acts as a normal backwards-facing step (BFS), where SWBLI and recirculation follow common trends. The ramp deflection of the BFSR geometry causes the flow structure to be more closely aligned with a compression corner. It is shown that for a BFS/BFSR with small deflection, downstream surface variable maxima increase with increased ramp deflection and decrease with increased Mach number and altitude. For a BFSR with large deflection, the opposite trends are seen.

Nomenclature

a	=	Speed of Sound
C_f	=	Coefficient of Skin Friction
C_h	=	Stanton Number
C_p	=	Pressure Coefficient
h	=	Step Height
M	=	Mach Number
P	=	Pressure
q	=	Dynamic Pressure
$\dot{q}$	=	Heat-Flux
Re	=	Reynolds Number
u, v	=	Velocity
y^+	=	Dimensionless Y-Coordinate
γ	=	Ratio of Specific Heats
δ_{99}	=	Boundary-Layer Thickness
δ_f	=	Deflection Angle
θ	=	Momentum Thickness
μ	=	Dynamic Viscosity
μ_t	=	Eddy Viscosity
$\tilde{\nu}$	=	S-A Variable
ρ	=	Density
τ	=	Shear Stress

*Graduate Student, School of Aeronautics and Astronautics, AIAA Student Member
†Associate Professor, School of Aeronautics and Astronautics, AIAA Associate Fellow
‡Professor, School of Aeronautics and Astronautics, AIAA Associate Fellow

I. Introduction

Computational fluid dynamics (CFD) has been a field for nearly 70 years, developing with the rise of numerical models and computational power. With the complexity of the Navier-Stokes equations, CFD has become a necessity to obtaining reliable solutions to complicated fluid dynamic problems. Experimental results can be analyzed with CFD methods allowing for quantization of entire flow fields and refinement of data that can not be obtained with conventional methods, such as pressure and heat-flux transducers. On the other hand, large geometries that can not be experimentally tested can benefit from CFD analysis, over basic analytic calculations, to reliably obtain data for complicated flow fields. Another important application is for fluid dynamic problems that have not yet been experimentally tested; these problems can utilize CFD to produce data to aid experimental design [1].

For this project, the latter application of CFD has been applied to a specific geometry. The project itself is split into two portions, the preliminary parametric study and the higher-fidelity study. The data produced for this paper will act as the parametric set of results. This set of data has been analyzed with flow structure and surface variable response as a primary focus. In future research we intend to use the results of this paper to continue investigation on a single, or several, specific sets of data. The overall objective of the project is to create a comprehensive analysis of this geometry, including higher-fidelity computations, for future experimental and aircraft design.

II. Problem Statement

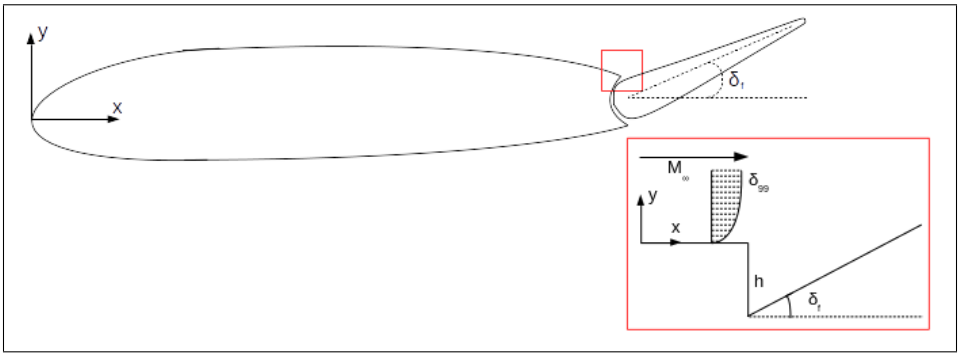

Fig. 1 Airfoil with Trailing-Edge Elevon

The particular area of interest for this project is the gap-region near the trailing-edge elevon of the wing. This is highlighted in Fig. 1, which depicts a cross-sectional view of the aircraft's wing, or an airfoil. This region is of particular interest because of the geometry that is inherently involved with a deflectable trailing-edge elevon. The trailing-edge of the airfoil is radiused to accommodate deflection, creating a curved channel, or cove, in this region. In order for this cove to exist, a small step is created between the trailing-edge of the airfoil and start of the cove. The cove-gap region then connects this step with the elevon. Research on this region is important because the cove environment can produce intolerable conditions for unprotected interior surface, seriously complicating effective design [2].

A. Idealization

In this preliminary work, the geometry was idealized for simplicity, by ignoring the gap and replacing the entire cove with just the small step. A schematic of this configuration is also shown in Fig. 1, where the parameters that characterize the flow are also represented. The 2-D idealized geometry is essentially a combination of two well-researched flow problem geometries, the backwards-facing step (BFS) and the compression corner. These two geometries will act as a basis to roughly define the problem for this study and to determine expected results. The first of the two problems is the BFS. The 2-D geometrical representation of the trailing-edge gap region converges to the exact backwards-facing step problem at zero ramp deflection. The BFS problem involves an inflow that reaches a sudden 90° downward surface deflection. This surface deflection will produce a recirculation region with a large vortex formed in the backward step region, producing a free shear layer which develops and attaches further downstream of the step. At reattachment, the flow turning produces weak expansion waves [3]. In the second problem, the compression corner, a similar surface deflection disrupts an inflow, however the deflection angle is acute and positive. This abrupt surface deflection leads to a generation of compression waves developing from the compression corner, which then interact with the

boundary-layer causing flow deceleration, and in turn, an adverse pressure gradient. The shock-wave boundary-layer interaction (SWBLI) at the compression corner not only causes separation but produces a free-shear layer which glides across the recirculation region and reattaches further downstream [4]. Collectively, the problem can be considered a backwards-facing step-ramp (BFSR).

B. Characteristic Flow Parameters

In order to develop a comprehensive set of data, a parametric study has to be defined. The parameters of interest are the characteristic flow parameters for this problem. When adjusted, these parameters will affect the flow structure and surface variable response. The characteristic flow parameters consist of boundary-layer thickness δ_{99}, momentum thickness θ, Reynolds number Re, ramp deflection δ_f, Mach number M_∞, and altitude. Freestream Mach number is coupled with the representative altitudes by applying a specific constant dynamic pressure in flight, establishing the freestream fluid properties and Reynolds number. This parameter affects the SWBLI that occurs near the step, thus affecting the generated shock, recirculation region, reattachment, and the recovering boundary-layer. Boundary-layer thickness and momentum thickness are coupled with Reynolds number, but can be adjusted by varying the running-length of the incoming flat-plate; however, this length was set to one meter for all cases. Ramp deflection angle was adjusted to match representative flight values and mainly affects the strength of the generated shock, which can be approximately determined by inviscid oblique shock relations. With the constant dynamic pressure relationship, the adjustable characteristic flow parameters reduce to Mach number and ramp deflection. Ramp deflection angles were set to representative values of 0°, 3°, and 10°. To match representative values for flight, Mach numbers were set to 2, 3, 4, 5, 6, and 7. These six values correspond to Cases 1, 2, 3, 4, 5, and 6, respectively. The remainder of the system is coupled to Mach number and altitude, establishing the parametric study for this paper.

C. Constant-q Trajectory

It would be unrealistic to have Mach number and altitude vary independently, as an aircraft has limitations that, for example, would not allow for effective flight at high Mach number and low altitude. Therefore, an approximate trajectory should be made to determine a representative Mach-altitude relationship. A simple trajectory model, outlined by DiGregorio [5], was used. Dynamic pressure, as a function of freestream Mach number and pressure, is defined as

$$q_\infty = \frac{1}{2} P_\infty M_\infty^2 \gamma, \tag{1}$$

where q_∞ is set to a representative constant value. To obtain atmospheric data to relate altitude with fluid dynamic pressure, the standard atmosphere tables were utilized [6]. The definition of dynamic pressure in Eq. 1 and the standard atmospheric data together establish the trajectory and Mach-altitude relationship. Keeping dynamic pressure constant in flight is viable as it would avoid large fluctuations in drag, as dynamic pressure is proportional to aerodynamic drag [7]. The resulting freestream information is tabulated for the selected cases along the trajectory in Table 1.

	Case 1	Case 2	Case 3	Case 4	Case 5	Case 6
Altitude, km	14.3	19.5	23.2	25.9	28.3	30.5
Mach	2.0	3.0	4.0	5.0	6.0	7.0
Pressure, kPa	13.39	5.92	3.33	2.18	1.51	1.09
Density, kg / m^3	0.216	0.095	0.053	0.034	0.023	0.017
Temperature, K	217	217	220	223	225	227
$Re \cdot 10^{-6}$, 1/m	8.94	5.92	4.37	3.52	2.86	2.39

Table 1 Approximate Trajectory Freestream Properties

An important note about constant dynamic pressure trajectory is the relationship that develops between Reynolds number and Mach number. Reynolds number, per unit length, can be defined as a function of Mach number

$$Re = \frac{\rho_\infty M_\infty a_\infty}{\mu_\infty}, \tag{2}$$

which is $\propto \rho_\infty M_\infty$, as speed of sound and dynamic viscosity have little atmospheric variance. With the constant-q relationship, the rate that atmospheric density drops is higher than the increase in Mach number at each step in the trajectory. Consequently, this produces an inverse relationship between Reynolds number and Mach number, where

$$Re \propto \frac{1}{M_\infty}. \tag{3}$$

III. Methodology

The numerical sets of data produced for this project were obtained with use of CFD software. As a result, the numerical set-up of the software will be outlined. The development of the employed computational grid will also be considered. The intent of this parametric study was not only to obtain accurate results from computations, but also to obtain precise results which can be readily compared. In order to ensure this, each computational case needs to be identical besides the parametric adjustments that are being made, requiring independent adjustment of the characteristic flow parameters. In addition, the general numerical setup, as well as the grid, should be identical in all computations.

A. Grid Generation

Any CFD computation requires a computational grid, or mesh, in order to run. The creation of a grid can be non-trivial and can negatively affect the computations. There is a give and take relationship between resolution and computational time, requiring that resolution needs to be refined and coarsened in various areas based on complexity of the flow area [8]. For wall-bounded flows, these regions are near the wall. For a flat-plate, resolution is needed at the start of the no-slip surface boundary. The incoming flat-plate requires sufficient resolution to capture the boundary-layer, specifically the viscous sublayer; this produces the wall-spacing constraint $\Delta y_w^+ \leq 1$. For a BFS, resolution should be high near the step's corner, separation region, and downstream reattachment. For a compression corner, high resolution is needed in the SWBLI region and the area of the shock itself. Considering the parametric study will involve multiple computations at a large range of Reynolds numbers, the grid had to be created to incorporate the differences in flow structure and needed resolution. Consequently, the final grid allowed for the thinnest vicious boundary-layer, the highest shock angle, and the largest recirculation region to be resolved.

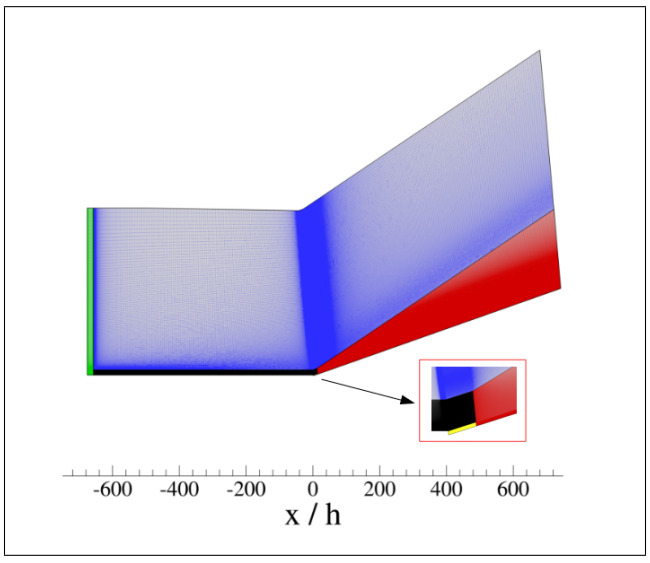

Fig. 2 BFSR Grid and Highlighted Zones

Fig. 2 visualizes the entirety of the grid and areas of higher resolution. The three main portions of the grid are the incoming flat-plate, the step, and the inclined ramp. For different degrees of deflection, 0°, 3°, and 10°, the inclined ramp section is simply rotated, providing easy transition between computations with a single grid. The grid is split into five independent zones, with corresponding resolution. On the far left side, the green-blue zonal interface requires an increase of resolution because of the flat-plate's no-slip surface. On the bottom of the flat-plate surface, the black zone

shows the highly resolved boundary-layer area. Further downstream, the grid resolution is refined before the start of the step for the same reasons as the start of the no-slip boundary, but there is no zonal changes. At the step and recirculation, the grid is most resolved as a combination of the black-yellow zones, shown with the zoomed-in red box in Fig. 2. This section is split into two zones at first, where the resolution required for the viscous sublayer and the step tip is redistributed to increase overall resolution of the downstream flow. These zones combine to form the red zone, where the resolution of the two are then widened again for downstream shock capturing. The blue zone shows the decreased resolution given to the non-changing freestream flow area. Nodal and cell information is tabulated in Table 2.

Zone	Color	X-Nodes	Y-Nodes	Z-Nodes	Cell Count
Inflow	Green	121	1283	2	153,840
Freestream	Blue	2766	200	2	550,235
Boundary-Layer	Black	1753	1084	2	1,897,416
Recirculation	Yellow	913	401	2	364,800
Shock Capturing	Red	1014	1484	2	1,502,279
Total	-	2886	1283-1683	2	4,468,570

Table 2 Grid Zonal and Cell Information

Considering that CFD results can be affected by the quality of the grid, a grid resolution study was done to determine if the total resolution is sufficient. As a result, before data was collected for the parametric study, two separate grids were introduced. The two grids, medium and coarse, were identical to the aforementioned grid, however resolution in most zones was decreased by a factor of two and three, respectively. Cases 2 and 4 acted as example computations for the two reduced-resolution grids. To test the effects of decreased resolution, downstream surface coefficient of skin friction and Stanton number were monitored. The conclusion of the study was that the original grid resolution was sufficient. The medium grid produced consistent results for skin friction and Stanton number, exceeding at most 1% and 5% difference in local magnitudes, respectively. The coarse grid produced at most 2% and 10% difference. The largest effect of resolution-reduction is seen in the recirculation region; far-downstream values converge to identical values.

B. Numerical Considerations

For this project, the commercial CFD software package GASP, developed by Aerosoft Inc., was employed. Initially, GASP was configured to obtain accurate solutions for high speed non-equilibrium flows. Currently, GASP has expanded its capabilities and now offers a wide variety of applicability [9, 10]. To obtain fluid dynamic results, GASP's Navier-Stokes solver was used. GASP's Navier-Stokes solver numerically operates as a Finite Volume Method (FVM) solver, where conservative variables are solved at cell centers, rather than nodes.

1. Turbulence Modeling

While the inviscid and viscous flux can be numerically computed, turbulence modeling must be done in order to pick up turbulent behaviors of the flow without relying on Direct Numerical Simulation (DNS) [11]. Turbulence modeling works by first separating the general Navier-Stokes equations into mean and instantaneous quantities, known as Reynolds-Averaging. With Reynolds-averaging, the variables associated with conservation equations can be decomposed, averaged, and simplified in order to obtain a statistical formation [12]. The turbulence model that was chosen for this paper was the Spalart-Allmaras (S-A) turbulence model. The S-A turbulence model is known for its robustness in comparison to other turbulence models. In addition, the model produces reliable data for wall-bounded and mixing layer flows [13, 14]. For GASP, the baseline and Detached Eddy Simulation (DES) versions of the S-A model are available. Future research for this project will make use of DES for computations. The S-A turbulence model is a one-equation model which solves the RANS equations, with use of an additional turbulence transport equation. This transport equation solves for the S-A turbulent variable $\tilde{\nu}$. This variable is used to compute the turbulent quantities of the flow, specifically the eddy viscosity, which is simply a function of the S-A variable and density $\mu_t = \rho\tilde{\nu}f_{v1}$. The transport equation itself is comprised of several coefficients and functions, such as f_{v1}, which come from validation of the model against experimental results [15].

C. Computational Configuration

The aim of this paper was to obtain a preliminary set of computations to be later investigated with higher-fidelity and time-accurate techniques. Certain numerical simplifications have been made. The first was that the RANS equations were employed, which is an approximation for turbulent calculations. The second was that the dimensionality of the problem was reduced to 2-D. Since GASP is a FVM solver, the grid itself must be 3-D; however, calculations are done at cell-centers, which allows a grid to function as 2-D if only two nodes exist in any dimension. The last was that steady-state solutions were sought, which ignores the unsteady affects of the flow. These simplifications reduce the computational time and power required to produce this set of data, while not completely changing the physics of the problem. GASP separates the inviscid flux and the viscous/turbulent flux equations. This allows the inviscid flux to be computed using techniques such as Advection Upstream Splitting Method (AUSM+) [16]. The molecular transport models define how thermodynamic properties are transported in a system. The following is a listed summery of the important specifications of the computational configuration.

1) Gas Species: Ideal Gas
2) Molecular Transport Properties: Sutherland Viscosity and Conductivity Model
3) Inviscid Flux Scheme: AUSM+ w/ MUSCL: 3rd Order Upwind Bias, Min-Mod limiter
4) Turbulence Model: Spalart-Allmaras (Baseline)
5) Temporal Scheme: Euler Implicit, Steady-State
6) Surface Boundary-Condition: Isothermal No-Slip Wall ($300K$)

The majority of data post-processing was done using two software packages. MATLAB was used for pure data analysis and manual calculations, and Tecplot was used for flow visualization and creation of figures.

IV. Results

The computational results obtained for this project were analyzed to investigate SWBLI, recirculation, and surface variable response. In total, three computational groups were created corresponding to each angle of ramp deflection. The angles of ramp deflection δ_f were taken to be 0°, 3°, and 10°. Each group was then split into six cases, where each case is another point along the approximate trajectory. This brings the total number of computations to 18. The layout of selected cases and corresponding freestream properties is located in *Section II: Problem Statement*, Table 1. The goal of the analysis of these results was two-fold, to develop a general understanding of the BFSR geometry in a representative flight trajectory and to determine key configurations for future investigation. The important parameters to characterize a boundary-layer are the boundary-layer thickness δ_{99}, momentum thickness θ, and Reynolds number Re_θ. The boundary-layer thickness is determined when the velocity of the boundary-layer roughly reaches $.99u_\infty$. The momentum thickness is calculated from the definition

$$\theta = \int_0^\infty \frac{\rho u}{\rho_\infty u_\infty}\left(1 - \frac{u}{u_\infty}\right) dy, \tag{4}$$

which is commonly used to set the length scale of the Reynolds number for the boundary-layer [17]. Due to the constant dynamic pressure trajectory, each of the cases holds an inverse relationship between Mach number and freestream pressure and density; the consequence of this is a drop in Reynolds number as Mach number, or altitude, is increased. This relationship leads to thinning of the boundary-layer and momentum thickness as Mach number and altitude increase. A table of these properties, taken at $x = -10h$ downstream, is provided in Table 3 for each case. Lastly, to better visualize shock structure and recirculation, contour plots in this section are plotted with an aspect ratio of 4:1.

	Case 1	Case 2	Case 3	Case 4	Case 5	Case 6
δ_{99}/h	11.8	11.5	10.9	10.1	9.1	8.9
θ/h	0.78	0.71	0.59	0.46	0.36	0.30
Re_θ	10600	6400	4000	2500	1600	1100

Table 3 Incoming Boundary-Layer Properties | x = -10h

A. SWBLI

SWBLI is the driving-feature of a compression corner flow, where the redirection of flow produces a shock wave which will interact with the boundary-layer and recirculation region. This interaction forms compression waves which emanate from recirculation and coalesce to form the single shock [18]. In contrast, flow expansion is the driving-feature of a BFS flow, where flow expands and increases in velocity as it turns over the downward deflection. For a BFS geometry, the flow turns again after the region of flow expansion to re-match the surface-angle, which leads to generation of weak compression waves [3]. For the group with ramp deflection of 0°, having no ramp deflection reduces the problem to a BFS geometry and thus completely resembles BFS flow. For positive ramp deflection, both SWBLI and expansion flow occur simultaneously, resulting in a complicated flow structure. In comparison to oblique shock theory

$$\frac{\rho_2}{\rho_1} = \frac{(\gamma+1)M_n^2}{(\gamma-1)M_n^2+2}, \tag{5}$$

the deflected cases show good agreement, with only small discrepancies as the Mach number and strength of the shock increase. Density ratios across the shock have been provided in Table 4 for each case and deflection angle, with comparison to Eq. 5. These values were taken post-interaction for all cases, at $x = -100h$, where ρ_1 and ρ_2 are average values taken before and after the shock. Both deflection angles produce similar difference with theory for each respective case. The largest percentage difference for both is attributed to Case 6, at roughly 2.4%.

	Case 1	Case 2	Case 3	Case 4	Case 5	Case 6
$\delta_f = 3°$	1.129	1.185	1.249	1.320	1.387	1.456
Eq. 5	1.126	1.176	1.233	1.294	1.356	1.421
Difference	0.3%	0.8%	1.3%	2.0%	2.3%	2.4%
$\delta_f = 10°$	1.464	1.665	1.905	2.162	2.435	2.691
Eq. 5	1.458	1.655	1.885	2.130	2.380	2.628
Difference	0.4%	0.6%	1.1%	1.5%	2.3%	2.4%

Table 4 Shock Density Ratio ρ_2/ρ_1 | x = -100h

1. BFS

The density contour plot provided in Fig. 3 is used to visualize the interaction for the BFS, 0° deflection, geometry. In each case of the BFS, the expansion waves are seen as a result of the step, redirecting the flow downwards. This interaction increases velocity of the flow while decreasing the flow's density. Flow is separated in the recirculation region and reattaches slightly further downstream. At the end of recirculation, weak compression waves develop as the flow is redirected again to match the surface angle. The shear-layer spreads downstream and reattaches at the end of recirculation. The size of the interaction is smaller on average than the BFSR geometry. Flow structure between cases are similar, but expectedly differ in the length of the interaction and strength/angle of the expansion waves.

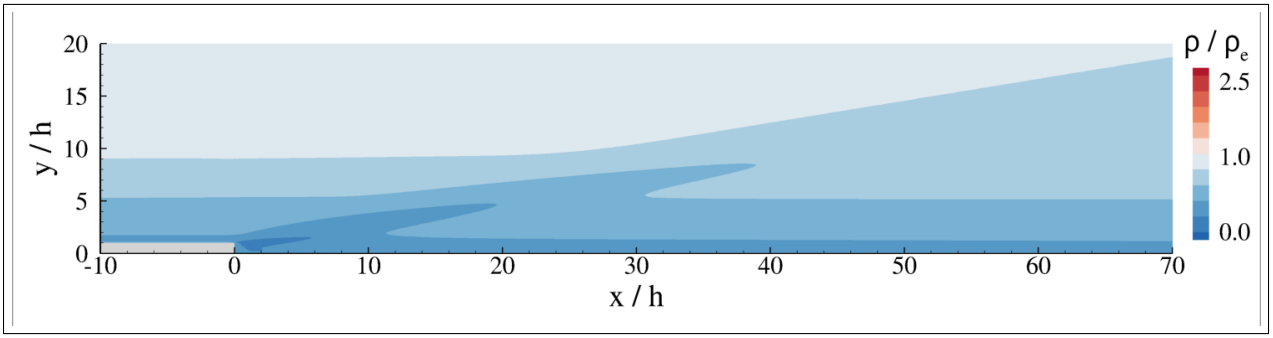

Fig. 3 Density Contour | Case 4, δ_f = 0°

2. BFSR

Fig. 4 provides a similar density contour plot for the BFSR geometry. Similar to the BFS, the flow expands over the step, leading to separation. The shear-layer also spreads downstream, reattaching at the end of recirculation. In contrast, the BFSR's deflection complicates the system by introducing an oblique shock. Near reattachment, expansion waves are met with strong emanating compression waves. Density of the flow downstream is compressed as a result of the upward turning flow. The strength and angle of the shock are strong functions of Mach number and turning angle, causing the interaction to change significantly between cases. The highest case numbers and ramp deflection angles produced the strongest interactions due to this relationship. The length of the interaction is affected by both the boundary-layer thickness and strength of the shock, but generally increased as Mach number and shock strength increased. The downstream flow for the BFSR geometry resembles compression corner flow. The recirculation region and reattachment are of particular interest for the project. In DDES computations of step-separated flow, the boundary-layer has been shown to breakdown into unsteady and turbulent flow after separation [19]. Future computations intend to capture this unsteadiness and resolve large turbulent structures post-separation.

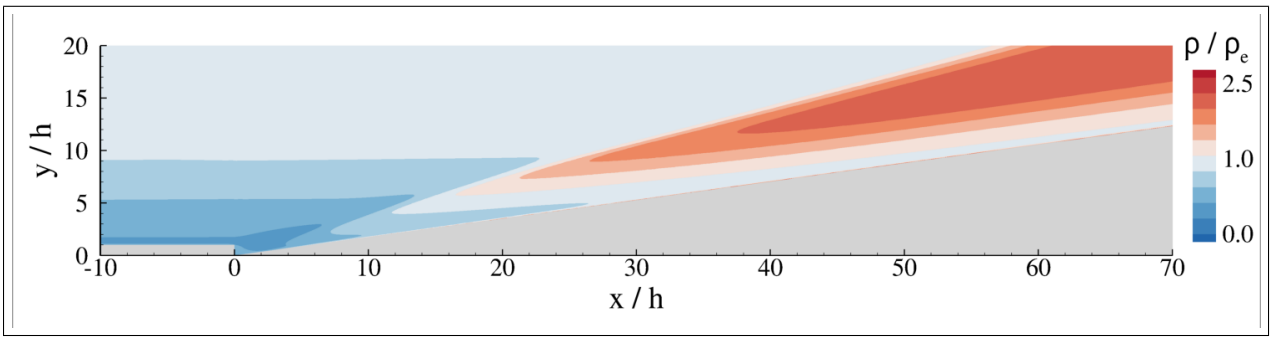

Fig. 4 Density Contour | Case 4, δ_f = 10°

B. Recirculation

The separation streamlines for both geometries show a similar structure of primary and secondary separation vortices, common to the BFS flow [20]. In most cases, the majority of the recirculation region consists of the primary vortex. The size of the secondary vortex is highly dependent on freestream properties and deflection angle, largely varying between computations. Flow reattachment location is the primary focus of this analysis and is tabulated in Table 5.

	Case 1	Case 2	Case 3	Case 4	Case 5	Case 6
δ_f = 0°	4.48	3.58	3.88	3.90	3.67	3.36
δ_f = 3°	4.95	3.62	3.95	4.23	4.46	4.58
δ_f = 10°	6.45	4.18	4.10	4.62	6.38	12.8

Table 5 Reattachment Length, x / h

1. BFS

Fig. 5 depicts the recirculation region and flow-turning for the BFS geometry. Without deflection, the flow is immediately separated after the step, extending downstream until reattachment. The recirculation region mainly consists of the primary separation vortex; the secondary separation vortex is generally much smaller. In most cases, the dividing line between the start of separation and reattachment is concave, where reattachment occurs 3.8h downstream on average. The separation streamlines for lower case numbers approached a convex structure, with larger secondary vortices. The BFS geometry always produced the smallest recirculation regions compared to the BFSR geometries. The flow's vertical v-velocity shown in Fig. 5 depicts the downward expansion flow over the step. Weak expansion waves turn the flow back to the angle of the surface, causing the v-velocity to approach zero after reattachment. The increase in downward v-velocity immediately downstream of the flow is the strongest for the BFS geometry, without strong compression waves.

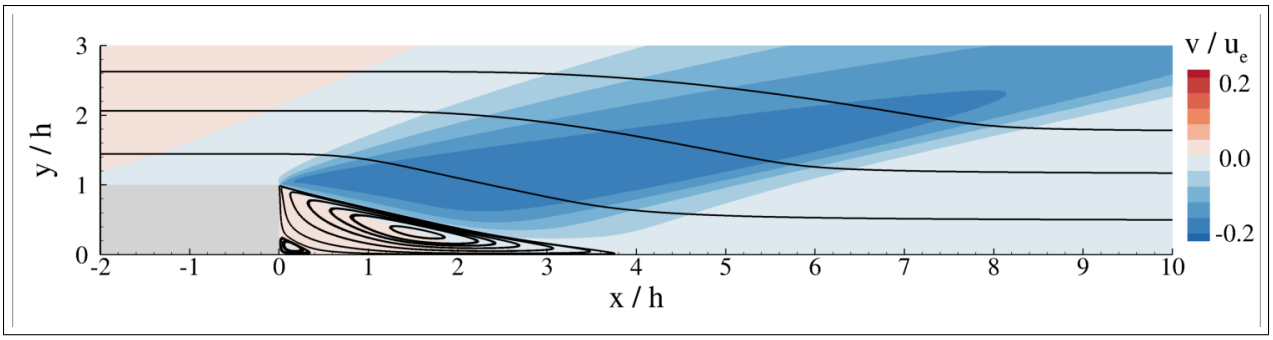

Fig. 5 Separation Streamlines & V-Velocity Contour | Case 4, δ_f = 0°

2. BFSR

Fig. 6 similarly depicts the flow structure and separation streamlines in the recirculation region for the BSFR geometry. The ramp deflection pushes the recirculation region upwards, having two general effects. The first is that the recirculation region is often elongated, where the angle of deflection is a strong factor. The second is change in the size and shape of the secondary separation vortex, which is also elongated and in some cases, slightly distorted. The secondary vortex is larger than that of the BFS geometry for similar cases. The dividing line between the start of separation and reattachment is concave for most cases; however, lower case numbers approach more convex structures similar to the BFS geometry. Reattachment occurs at $4.3h$ downstream on average for 3° deflection and $5.1h$ downstream on average for 10° deflection. The effect of SWBLI in this region is also depicted in Fig. 6. The deflection of the downstream ramp restricts the turning angle of the flow, producing weaker expansion waves than the BFS geometry. At reattachment, expansion waves meet stronger compression waves than the BFS, due to ramp deflection. The positive.v-velocity also results from ramp deflection.

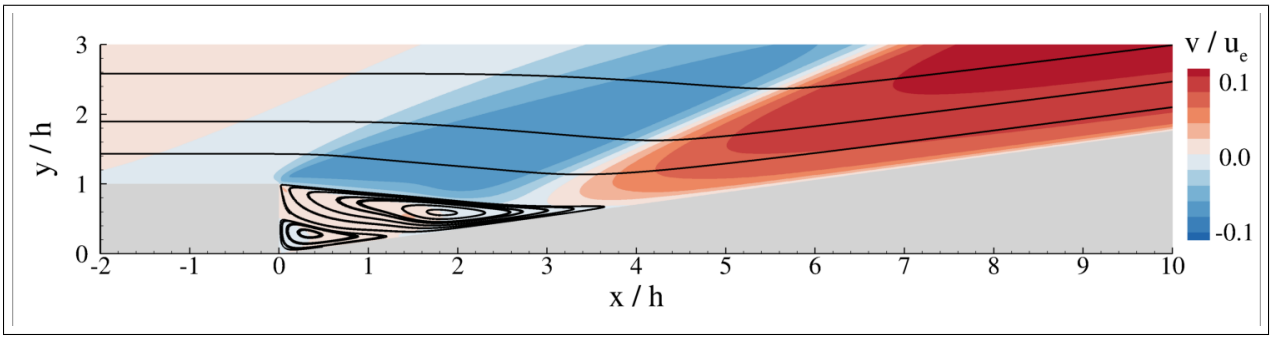

Fig. 6 Separation Streamlines & V-Velocity Contour | Case 4, δ_f = 10°

C. Surface Variable Response

The response of surface variables corresponding to each computational case was another primary focus of this project. The intended goal is to obtain trends that correspond with the various adjustments made throughout the project. The surface variables that were of interest are those that can be related to aerodynamic drag and heat transfer. For the BFS geometry, drag is due to skin friction, whereas the ramp deflection of the BFSR geometry also produces wave drag. To reliably compare response at the surface between cases with different freestream properties, non-dimensional variables were sought. The non-dimensional surface variables that were analyzed were the coefficient of skin friction

$$C_f = \frac{\tau_w}{q_\infty}, \tag{6}$$

the Stanton number, as defined by GASP,

$$C_h = \frac{\dot{q}}{\rho_\infty u_\infty \left(h_{o,\infty} - h_{o,w}\right)}, \tag{7}$$

and the pressure coefficient

$$C_p = \frac{P - P_\infty}{q_\infty}. \tag{8}$$

1. Coefficient of Skin Friction

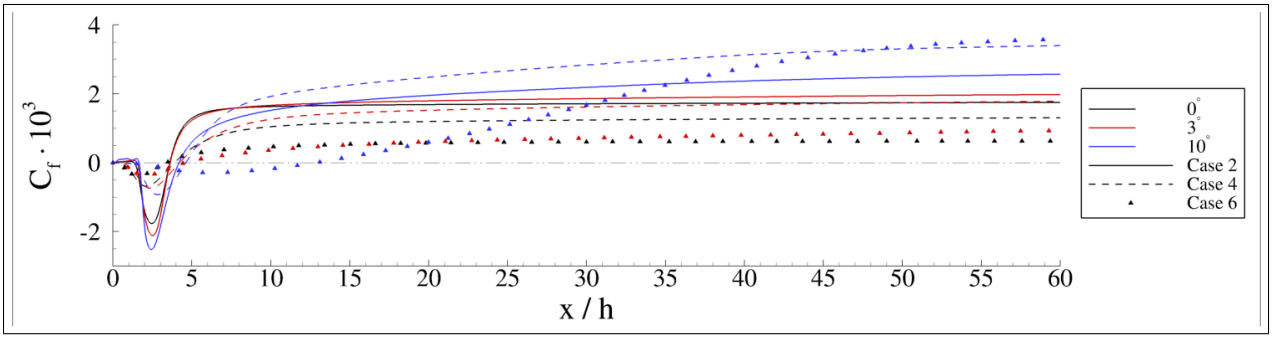

Fig. 7 Coefficient of Skin Friction, $C_f \cdot 10^3$

Fig 7 shows the trend of skin friction along the downstream ramp of the BFS and BFSR geometries. Separation and reattachment locations can be seen as skin friction drops below and increases above zero. After reattachment, skin friction sharply increases, reaches a maximum value, and then gradually decreases downstream as the boundary-layer thickens. To obtain significant tabulated data for comparison, maxima were taken post-interaction. The resultant maxima are tabulated in Table 6. Several trends can be identified from the response of skin friction throughout each case and ramp deflection. Skin friction maxima are shown to increase with deflection angle, where higher case numbers produced much larger differences between deflection angles. For the BFS and 3° BFSR geometries, skin friction maxima decreased with an increase in Mach number and altitude. For the 10° BFSR geometry, skin friction maxima increased with an increase of Mach number and altitude. The largest difference between geometries is seen in Case 6, where maximum skin friction for the 10° BFSR is four times larger than the BFS and two times larger than the 3° BFSR.

	Case 1	Case 2	Case 3	Case 4	Case 5	Case 6
$\delta_f = 0°$	1.91	1.78	1.60	1.36	1.12	0.84
$\delta_f = 3°$	2.03	2.07	2.01	1.87	1.65	1.40
$\delta_f = 10°$	2.31	2.86	3.25	3.54	3.72	3.65

Table 6 Tabulated Coefficient of Skin Friction Maxima, $C_f \cdot 10^3$

2. Stanton Number

Fig. 8 depicts the Stanton number along the downstream ramp. The computations employ a cooled wall, which causes heat-flux into the surface, resulting in negative values for the Stanton number. The Stanton number behaves slightly different than the coefficient of skin friction. For the BFS geometry, the Stanton number sharply increases in separation, peaks near reattachment, then gradually decreases downstream. The BFSR geometry produces a similar behavior, however the peak is reached post-interaction. To obtain significant tabulated data for comparison, respective maxima were taken for each geometry and case and tabulated in Table 7. The general trends in Stanton number are equivalent to that of skin friction. Stanton number maxima increased with ramp deflection, where higher case numbers similarly produced much larger differences between deflection angle. This difference is larger than that of skin friction.

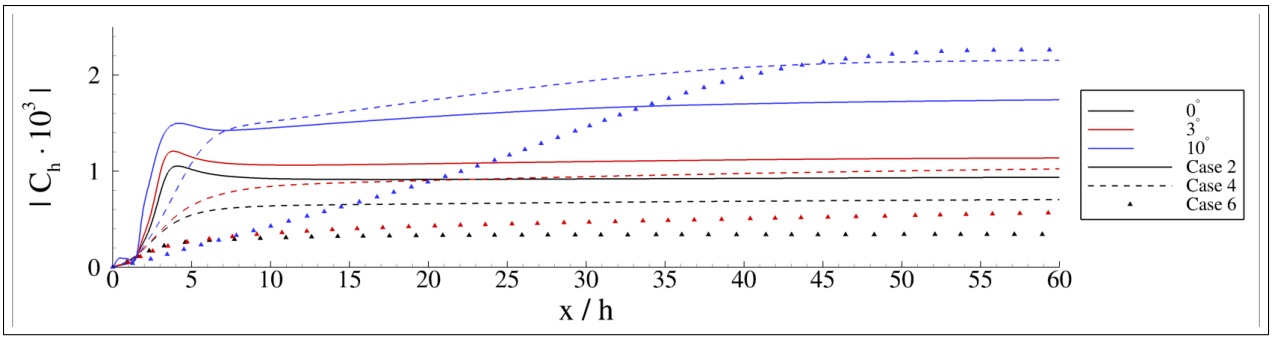

Fig. 8 Stanton Number, $C_h \cdot 10^3$

The largest difference is also seen in Case 6, where maximum Stanton number values for the 10° BFSR geometry were five times larger than the BFS and three times larger than the 3° BFSR. The three geometries also produced differing relationships with Mach number and altitude. For the BFS and 3° BFSR geometries, Stanton number maxima decreased with an increase in Mach number and altitude. In contrast, the Stanton number maxima for the 10° BFSR generally increased with an increase in Mach number and altitude.

$\cdot 10^3$	Case 1	Case 2	Case 3	Case 4	Case 5	Case 6
$\delta_f = 0°$	1.08	1.05	0.85	0.73	0.60	0.45
$\delta_f = 3°$	1.17	1.20	1.12	1.05	0.91	0.76
$\delta_f = 10°$	1.46	1.48	1.98	2.16	2.29	2.26

Table 7 Tabulated Stanton Number Maxima, $C_h \cdot 10^3$

3. Pressure Coefficient

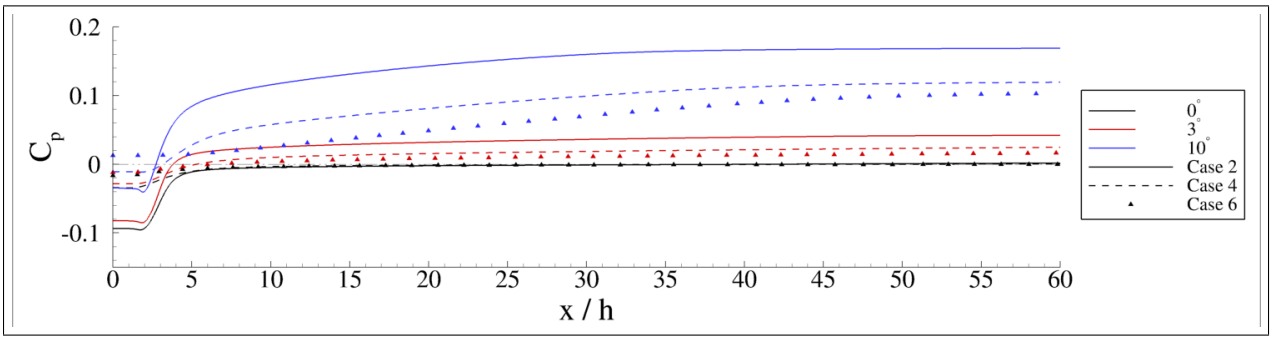

Fig. 9 Pressure Coefficient, $C_p \cdot 10^3$

The pressure coefficient acts to differentiate the BFS and BFSR geometries, provided in Fig. 9. For the BFS geometry, the pressure coefficient starts negative, sharply rises in recirculation, then plateaus to a near-zero value downstream. For the BFSR geometry, the trend in the pressure coefficient follows that of a compression corner, in that the sharp rise in recirculation exceeds zero and gradually plateaus to a non-zero value. The rise in the pressure coefficient for the BFSR geometry is attributed to the increase in downstream pressure caused by the shock.

Downstream results can be compared to theory to determine general affect of the step-ramp interaction. The theoretical inviscid pressure coefficient, as a function of Mach number and shock pressure ratio, is

$$C_{p,inv} = \frac{2}{\gamma M_\infty^2}\left(\frac{P_2}{P_\infty} - 1\right). \tag{9}$$

Theoretical C_p values calculated with Eq. 9 and percentage differences are tabulated along with downstream values for all cases in Table 8. Comparatively, the downstream pressure coefficient for the 10° BFSR showed smaller percentage difference with theory than the 3° BFSR. The 3° and 10° geometries averaged at 6.5% and 3% difference, respectively.

	Case 1	Case 2	Case 3	Case 4	Case 5	Case 6
δ_f = 3°	0.067	0.043	0.033	0.027	0.023	0.021
Eq. 9	0.065	0.041	0.031	0.025	0.021	0.019
Difference	3.8%	4.5%	5.6%	7.7%	9.1%	8.1%
δ_f = 10°	0.256	0.170	0.138	0.120	0.110	0.104
Eq. 9	0.252	0.167	0.134	0.117	0.106	0.099
Difference	1.6%	1.8%	2.9%	3.4%	3.7%	4.9%

Table 8 Tabulated Pressure Coefficient, C_p | x = -60h

D. Outlying Case

While overall flow structure differences and general trends in surface response between the BFS and BFSR geometries can be drawn from Cases 1-5, one particular case presented different results. The last case, Case 6, which represents high Mach number flow at low Reynolds number, deviated from the flow structure seen in previous cases when deflected by 10°. This interaction presents two major differences, which are the location of the oblique shock and the size of recirculation. For this particular configuration, the shock interacts with boundary-layer upstream of the step, compared to downstream near reattachment. This extends the compression waves further back, causing a larger interaction. This SWBLI is visualized in Fig. 10, which is distinctly different from the previous configurations. The reason for this departure from other cases is likely a factor of the very strong shock caused by the high Mach number flow, as well as the low Reynolds number of the boundary-layer. Additionally, this shock alters the structure of the recirculation region. The oblique shock produces separation prior to the step, causing the entire step to be engulfed in the recirculation region. This recirculation region is heavily elongated when compared to other cases, doubling in length from its average size. The surface response also deviates from cases for this configuration. Referring back to the previous subsection, the trends developed in the coefficient of skin friction and the Stanton number do not hold. However, the pressure coefficient trends hold regardless of this change in flow structure. The nature of this interaction is intriguing, as it is the only case which produced significant differences in flow structure.

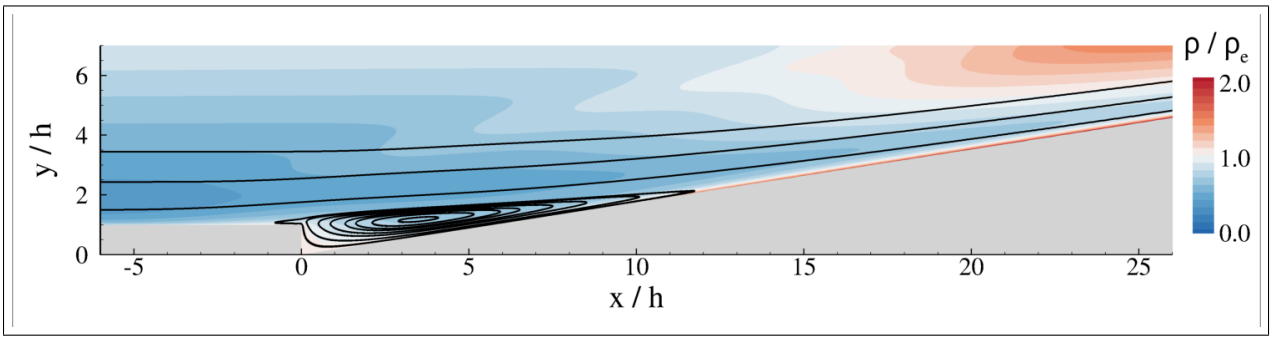

Fig. 10 Separation Streamlines & Density Contour | Case 6, δ_f = 10°

V. Concluding Remarks

The intent of this paper was to develop an initial understanding of the BFSR geometry in a representative flight trajectory. This has been done with a parametric study in order to produce a set of preliminary data. The flow structure of the BFSR geometry is similar to both the BFS and compression corner geometries, but has a stronger similarity to the compression corner. Increases of Mach number and altitude, with decreasing Reynolds number, produced shock waves with strengths in agreement with inviscid oblique shock theory. The location of reattachment is found to roughly occur from $3h$ up to $6h$ for most cases. Surface variable response trends show a general relationship between the coefficient of skin friction, Stanton number, and pressure coefficient with ramp deflection. This relationship depicts large increases of surface variables with increases of ramp deflection. These variables show weak trends between surface variable response and Mach number and altitude. It can be seen that low deflection angles only slightly affect the surface variable response when compared to the BFS geometry, where large deflection angles produced larger responses. The 0° and 3° BFSR geometries show decreases in surface variable response with increasing Mach number and altitude. The 10° geometry shows a reverse relationship, where surface variable response generally increases with increasing Mach number and altitude. Collectively, the relationships that arose between the differing cases and geometries paints a general picture of the responses of the system to freestream quantities, inflow Mach number, and ramp deflection angle. The outlying case, however, produces a different flow structure than any of the other cases.

The idealizations and simplifications of this project have affected the final results in several ways. The reattachment position is inherently unsteady, resulting in inaccurate predictions with steady-state RANS solutions. The use of the baseline S-A turbulence model does not allow for resolution of turbulent structures in the boundary-layer, affecting the shear-layer entrainment rate and separation angle at the step [19]. Three-dimensionality also plays a significant role in flow separation and is expected to show significant differences from pseudo two-dimensional computations. Therefore, research presented in this paper will be continued on the BFSR geometry by reducing idealization and applying higher-fidelity techniques. To allow for a more intensive investigation of this flow configuration and geometry, the simplifications made to the system will be removed. Geometrically, this will extend the computational domain to three-dimensions. In addition, physical gap and elevon cove region outlined in the *Section I: Introduction* will be added to reduce to the idealization of the cross-sectional geometry. Numerically, unsteady solutions will now be sought, which will change the temporal integration. The turbulence modeling for this project will be changed from the one-equation S-A model to Detached Eddy Simulation (DES). DES acts as a combination of both Reynolds-Averaged Navier-Stokes (RANS) and Large Eddy Simulation (LES); the near-wall regions are modeled by basic RANS, whereas regions far from the wall are modeled with LES [21]. The intent of the future research is to continue the investigation of the BFSR geometry, where higher-fidelity techniques and reduction of idealization will allow for more accurate computations. The addition of unsteadiness and LES will also now allow for spectral content to be analyzed. The primary configuration for future research will be the outlying case, Case 6 with 10° deflection, due to its distinctly different flow structure.

Acknowledgments

The present work was supported by AFRL under the "Reusable Hypersonic Vehicle Structures" project, Contract FA8650-18-c-2253. Computational resources were provided by the AFRL DSRC and by Information Technology at Purdue, West Lafayette, Indiana. Cleared for public release on November 19, 2019 under case number 88ABW-2019-5622.

References

[1] Jameson, A., "Computational Fluid Dynamics Past, Present and Future," Technical Report, Stanford University, 2012.

[2] Deveikis, W., and Bartlett, W., "Pressure and Heat-Transfer Distributions in a Simulated Wing-Elevon Cove with Variable Leakage at a Free-Stream Mach Number of 6.9," Technical Report, Langley Research Center, 1978.

[3] Chen, L., Asai, K., Nonomura, T., Xi, G., and Liu, T., "A Review of Backward-Facing Step (BFS) Flow Mechanisms, Heat Transfer and Control," *Thermal Science and Engineering Progress*, Vol. 6, 2018.

[4] Bibin, J., Kulkarni, V., and Natarajan, G., "Shock Wave Boundary Layer Interactions in Hypersonic Flows," *International Journal of Heat and Mass Transfer*, Vol. 70, 2014.

[5] DiGregorio, N., "Characteristics of Turbulent Boundary Layers Along a Hypersonic Vehicle," Master's thesis, State University of New York at Buffalo, 2018.

[6] United States Committee on Extension to the Standard Atmosphere, *U.S. Standard Atmosphere*, National Oceanic and Atmospheric Administration, 1976.

[7] Long, L. N., and Weiss, H., "The Velocity Dependence of Aerodynamic Drag: A Primer for Mathematicians," *The American Mathematical Monthly*, Vol. 106, No. 2, 1999, pp. 127–135.

[8] Daud, H. A., Li, Q., Bég, O., and AbdulGhani, S., "Numerical Investigations of Wall-Bounded Turbulence," *Proceedings of the Institution of Mechanical Engineers, Part C: Journal of Mechanical Engineering Science*, Vol. 225, No. 5, 2011, pp. 1163–1174.

[9] McGrory, W., Huebner, L., Slack, D., and Walters, R., "Development and Application of GASP 2.0," *4th Symposium on Multidisciplinary Analysis and Optimization*, 1992.

[10] Neel, R., Godfrey, A., and Slack, D., "Turbulence Model Validation in GASP Version 4," *33rd AIAA Fluid Dynamics Conference and Exhibit*, 2012.

[11] Reynolds, W. C., *Fundamentals of Turbulence for Turbulence Modeling and Simulation*, 1987.

[12] Wilcox, D., *Turbulence Modeling for CFD*, 3rd ed., DCW Industries, Inc., 2006.

[13] Paciorri, R., Dieudonne, W., Degrez, G., Charbonnier, J.-M., Deconinck, H., Paciorri, R., Dieudonne, W., Degrez, G., Charbonnier, J.-M., and Deconinck, H., "Validation of the Spalart-Allmaras Turbulence Model for Application in Hypersonic Flows," *28th Fluid Dynamics Conference*, 1997.

[14] Bardina, J., Huang, P., Coakley, T., Bardina, J., Huang, P., and Coakley, T., "Turbulence Modeling Validation," *28th Fluid Dynamics Conference*, 1997.

[15] Spalart, P., and Allmaras, S., "A One-Equation Turbulence Model for Aerodynamic Flows," *30th Aerospace Sciences Meeting and Exhibit*, 1992.

[16] *GASPex Technical Reference Guide*, Blacksburg, VA, 2011.

[17] Smits, A. J., "Turbulent Boundary-Layer Structure in Supersonic Flow," *Philosophical Transactions: Physical Sciences and Engineering*, Vol. 336, No. 1641, 1991, pp. 81–93.

[18] Green, J., "Interactions Between Shock Waves and Turbulent Boundary Layers," *Progress in Aerospace Sciences*, 1970, pp. 235–340.

[19] Leger, T., Bisek, N., and Poggie, J., "Detached-Eddy Simulation of a Supersonic Reattaching Shear Layer," *AIAA Journal*, Vol. 55, No. 11, 2017, pp. 3722–3733.

[20] Halupovich, Y., Natan, B., and Rom, J., "Numerical Solution of the Turbulent Supersonic Flow Over a Backward Facing Step," *Fluid Dynamics Research*, Vol. 24, No. 5, 1999, pp. 251 – 273.

[21] Pope, S., *Turbulent Flows*, 1st ed., Cambridge University Press, 2000.